

# A detection of the secondary eclipse of Qatar-1b in the Ks-band <sup>★</sup>

Patricia Cruz<sup>1,2</sup>, David Barrado<sup>2</sup>, Jorge Lillo-Box<sup>3,2</sup>, Marcos Diaz<sup>1</sup>, Jayne Birkby<sup>4,5</sup>, Mercedes López-Morales<sup>4</sup>, Jonathan J. Fortney<sup>6</sup>

<sup>1</sup> Instituto de Astronomia, Geofísica e Ciências Atmosféricas, Universidade de São Paulo (IAG/USP), São Paulo, Brazil  
e-mail: patricia.cruz@iag.usp.br

<sup>2</sup> Depto. de Astrofísica, Centro de Astrobiología (INTA-CSIC), ESAC campus, Camino Bajo del Castillo s/n, E-28692, Villanueva de la Cañada, Spain

<sup>3</sup> European Southern Observatory (ESO), Alonso de Cordova 3107, Vitacura, Casilla 19001, Santiago de Chile, Chile

<sup>4</sup> Harvard-Smithsonian Center for Astrophysics, 60 Garden Street, Cambridge, MA 02138, USA

<sup>5</sup> NASA Sagan Fellow

<sup>6</sup> Department of Astronomy and Astrophysics, University of California, 1156 High Street, Santa Cruz, CA 95064, USA

Received XXXXX; accepted XXXXX

## ABSTRACT

**Aims.** Qatar-1b is a close-orbiting hot-Jupiter ( $R_p \approx 1.18 R_J$ ,  $M_p \approx 1.33 M_J$ ) around a metal-rich K-dwarf, with orbital separation and period of 0.023 AU and 1.42 days, respectively. We have observed the secondary eclipse of this exoplanet in the Ks-band with the objective of deriving a brightness temperature for the planet and providing further constraints to the orbital configuration of the system.

**Methods.** We obtained near-infrared photometric data from the ground by using the OMEGA2000 instrument at the 3.5 m telescope at Calar Alto (Spain), in staring mode, with the telescope defocused. We have used Principal Component Analysis (PCA) to identify correlated systematic trends in the data. A Markov chain Monte Carlo analysis was performed in order to model the correlated systematics and fit for the secondary eclipse of Qatar-1b using the occultation model by Mandel & Agol (2002).

**Results.** We measured a secondary eclipse depth of  $0.196\%_{-0.051\%}^{+0.071\%}$ , which indicates a brightness temperature in the Ks-band for the planet of  $1885_{-168}^{+212}$  K. We also measured a small deviation in the central phase of the secondary eclipse of  $-0.0079_{-0.0043}^{+0.0162}$ , which leads to a value for  $e \cos \omega$  of  $-0.0123_{-0.0067}^{+0.0252}$ . However, this last result should be confirmed with more data.

**Conclusions.** This work highlights that ground-based secondary eclipse observations are capable of providing useful constraints on the orbital configuration of bright, giant planets that can be used to probe the architecture and multiplicity in hot Jupiter systems.

**Key words.** planetary systems – stars: individual (Qatar-1b) – technique: photometry

## 1. Introduction

Qatar-1b is a close-orbiting hot-Jupiter, with an initially measured planetary radius of  $R_p = 1.164 \pm 0.045 R_J$  and a mass of  $M_p = 1.090_{-0.081}^{+0.084} M_J$  (Alsubai et al. 2011). It orbits its central star, a metal-rich K-dwarf, with a period of approximately 1.42 days, and an orbital separation of  $0.02343_{-0.00025}^{+0.00026}$  AU. This exoplanet was firstly assumed to be in a circular orbit (fixed  $e = 0.0$ ; Alsubai et al. 2011).

Covino et al. (2013) published five new transit epochs, which combined with previous data from Alsubai et al. (2011) resulted in new ephemerides and improved parameters for Qatar-1b system ( $R_p = 1.18 \pm 0.09 R_J$ ;  $M_p = 1.33 \pm 0.05 M_J$ ). These authors also presented a revised orbital solution for this object, based on 11 radial velocity (RV) measurements, finding an eccentricity of  $e = 0.020_{-0.010}^{+0.011}$ . They also observed the Rossiter-McLaughlin effect in the RV curve, determining the sky-projected obliquity and concluding that the system is well-aligned.

In addition, von Essen et al. (2013) reported indications of long-term transit timing variations (TTVs) based on 26 transits. In order to explain the observed  $\sim 190$  days TTV period, these authors presented different cases that could be responsible for such variations. One of the possibilities would be the presence

of a weak perturber in resonance with Qatar-1b, since two planetary bodies in resonance would experience long-term variations in their orbital parameters. In contrast, very recent works by Mislis et al. (2015) and Maciejewski et al. (2015) did not find conclusive evidences of TTVs. Nevertheless, Mislis et al. (2015) indicated that more precise data are needed for further conclusions.

In this paper we present the second result of the Calar Alto Secondary Eclipse study (the CASE study; see Cruz et al. 2015): a detection of the secondary eclipse of Qatar-1b in Ks-band, with the goal of measuring its Ks-band thermal emission for the first time. We also aim to constrain the planet's orbital configuration by looking for offsets in the mid-eclipse timing that would indicate a non-circular orbit and possible perturbations. This paper is divided as follows: in Sect. 2 we present the data acquisition and the reduction procedures applied to them; in Sect. 3 we describe our analysis, including the correction of systematic effects and the modeling of the eclipse, and the fitting results; in Sect. 4 we discuss the thermal emission and the orbital configuration of Qatar-1b; in Sect. 5 we present our conclusions.

## 2. Observations and data reduction

Qatar-1 ( $K=10.409$  mag) was observed in service mode on the night of 2011 August 30, under photometric conditions. This

<sup>★</sup> Based on observations collected at the Calar Alto Observatory, Almería, Spain.

**Table 1.** Reference stars used for the relative photometry.

Star No.	Identifier (2MASS)	K mag
1	J20142800+6506270	9.231
2	J20131440+6507000	10.560
3	J20142873+6507445	9.584
4	J20123648+6508138	9.254
5	J20141068+6511408	10.674
6	J20133795+6512408	10.643
7	J20140978+6512548	8.995
8	J20125213+6514365	9.347
9	J20135707+6515082	8.879

night was selected by estimating the occurrence of a secondary eclipse, assuming a circular orbit<sup>1</sup>. We used the Ks-band filter (centred on  $2.14 \mu\text{m}$ ) of the OMEGA2000 instrument equipped with a  $2k \times 2k$  HAWAII-2 detector, on the 3.5 m telescope at the Calar Alto Observatory (CAHA) in southern Spain. The field of view is of  $15.4 \times 15.4$  arcmin and the plate scale of  $0.45 \text{ arcsec pix}^{-1}$ . In order to reduce intrapixel variations and minimize the impact of flat-field errors, the telescope was arbitrarily defocused, resulting in a ring-shaped PSF with a mean radius of  $\sim 4.45 \text{ arcsec}$  (around 10 pixels, approximately). The relative photon noise in a single raw defocused image is of  $\sim 4.6 \times 10^{-3}$ .

We acquired the data in staring mode, observing continuously the target without dithering. Such technique has been used for similar purposes by several authors, for example, Croll et al. (2010a, 2010b, 2011), de Mooij et al. (2011), Cruz et al. (2015). We gathered a series of data where every file has 15 images of 4s exposure each ( $190 \times 15 \times 4s$ + overheads), totaling 2850 individual measurements with an average cadence of  $\sim 11.3$  images per minute. A manual guiding correction was performed, keeping the stars as much as possible on the same position on the detector. These staring mode observations were collected during approximately 4.2 hours. Before and after this sequence, in-focus images composed by 5 dither-point images each were also obtained for further sky subtraction. The data reduction was performed using IRAF<sup>2</sup> for the bad pixel removal, flat-fielding and sky subtraction, which are described in detail in Cruz et al. (2015).

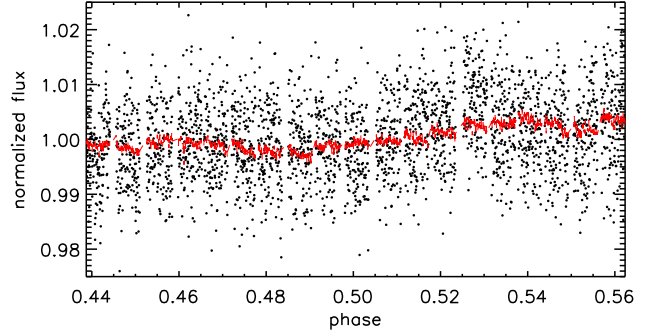
We performed aperture photometry in each image using the *aper* procedure from the IDL Astronomy User's Library<sup>3</sup>. We selected a circular aperture with a radius of 12.5 pixels and inner and outer annuli of 19.5 and 36.5 pixels, respectively, to measure the residual sky background. For the photometry, we tested different apertures from 3 to 25 pixels, in steps of 0.5 pix. We used the aperture that presented a maximum signal-to-noise ratio for the target. Sky annuli were also varied by several pixels, but had negligible effect on the final photometry.

Table 1 shows the stars used as reference for the differential photometry. These stars were selected because they did not present any strong variations nor other odd behavior in their light curves.

<sup>1</sup> The secondary eclipse timing, assuming a circular orbit, was predicted with the help of the Exoplanet Transit Database, ETD, maintained by the Variable Star Section of Czech Astronomical Society - for more details, <http://var2.astro.cz/ETD/index.php>.

<sup>2</sup> IRAF is distributed by the National Optical Astronomy Observatory, operated by the Association of Universities for Research in Astronomy, Inc., under cooperative agreement with the National Science Foundation.

<sup>3</sup> IDL stands for Interactive Data Language - for further information, see <http://www.itvis.com/ProductServices/IDL.aspx>; *aper.pro* is distributed by NASA - see <http://idlastro.gsfc.nasa.gov/> for more details.



**Fig. 1.** Uncorrected differential light curve of Qatar-1 in the Ks-band shown in phase. The thin line represents the best model obtained from the joint-MCMC.

The relative flux of Qatar-1 was calculated by its measured flux,  $F_{\text{tar}}(t)$ , over the sum of the flux of all reference star considered, and then normalized by its median value, as follows:

$$F(t) = \frac{F_{\text{tar}}(t)}{\sum_{i=1}^9 F_{\text{ref},i}(t)}, \quad (1)$$

$$f(t) = \frac{F(t)}{\bar{F}}, \quad (2)$$

where  $F_{\text{ref},i}(t)$  is the measured flux of reference star  $i$ , at a given time  $t$ ,  $\bar{F}$  is the median value of target's relative flux estimated from the expected out-of-eclipse section of the light curve, and  $f(t)$  is the normalized flux of the target. The differential light curve of Qatar-1 is shown in Fig. 1.

### 3. Data analysis and results

The analysis of the data presented here followed the steps presented in the previous paper of this series (Cruz et al. 2015). We maintained the same procedure in order to obtain an homogeneous analysis, having coherence between the results.

#### 3.1. Correction of systematic effects

In order to clean the light curve from systematic effects, we have searched for correlations between the observed flux and several other parameters. We have used the Principal Component Analysis (PCA) technique<sup>4</sup>, a powerful statistical tool for dimensional evaluation in data sets, in order to identify the systematics that have a direct impact on the data (for more details, see Cruz et al. 2015). This method was primarily used to recognize which variables are responsible for most of the variance in the data set. The purpose here was to identify the parameters that strongly affect the data. It is worth emphasizing, at this point, the data is not yet corrected from systematics. The parameters with a high eigenvalue are selected for a posterior elimination of the dominant patterns without compromising the eclipse signal.

We have calculated the PCAs for a few reference stars listed in Table 1. Those stars with similar 2MASS colors were selected to minimize differential refraction and other chromatic effects. They were treated separately, with their normalized fluxes obtained from Eq.1 and 2, where  $F_{\text{tar}}$  is the measured flux of

<sup>4</sup> In a  $R^n$  array, the PCA finds the linear combination (vector) of  $n$  axes that best reproduces the data distribution in question. For more, see Morrison (1976).

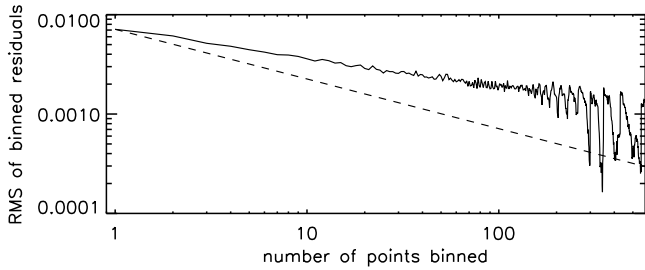


**Fig. 2.** RMS of the residuals of the out-of-eclipse portion of the light curve, for different bin sizes. The dashed line shows the limit expectation for normally distributed noise.

the reference star. We have analyzed different reference light curves, where we excluded the star in question from the sum in Eq. 1 when dealing with a particular reference star. These analyses have revealed significant correlations of the normalized flux with star’s xy-position of the centroid at the detector ( $x_c$ ,  $y_c$ ), “defocused seeing”<sup>5</sup> ( $s$ ), and airmass (sec  $z$ ). The behavior of these parameters as function of the orbital phase is presented in Appendix A. The light curves of the reference stars were considered only for the identification of the systematics, and were not used for the analysis of the light curve of Qatar-1. We also have calculated the PCAs for Qatar-1, and we have found correlations with the same parameters. For this, we have considered only the expected out-of-eclipse (*ooe*) part of the light curve, assuming a circular orbit, where the stellar flux is supposed to be constant.

Thereafter, we have performed a multiple linear regression in IDL (*regress*), fitting for these systematics simultaneously, generating a polynomial of the form:

$$f_{\text{ooe}} = c_0 + c_1 x_{c,\text{ooe}} + c_2 y_{c,\text{ooe}} + c_3 s_{\text{ooe}} + c_4 \sec z_{\text{ooe}}. \quad (3)$$

Here,  $f_{\text{ooe}}$  is the out-of-eclipse flux of the target and  $c_k$  are constants of the fit. This linear regression was performed only in the expected out-of-eclipse part of the light curve to avoid the removal of eclipse signal along with systematics. This correction function was determined by using the light curve of the target only, and corrected point by point considering the xy-position of the target in order to assess the behavior of the residuals. From the out-of-eclipse portion of the decorrelated unbinned light curve, we estimated a root-mean-square, RMS, of  $\sim 7.1 \times 10^{-3}$ .

We show in Figure 2 the behavior of the residuals. The expected Gaussian noise, defined as one over the square-root of the bin size, is also presented for comparison. Considering only the expected out-of-eclipse data, we have explored the noise level (RMS) behavior by binning the curve with different bin sizes, from 1 to 580 points per bin from a total of 1761 out-of-eclipse individual measurements. In the latest case, the binned light curve would have only three points. The RMS of the residuals is higher than the white noise, which we attribute to the presence of significant correlated noise in the photometric data.

We have analyzed the power spectrum of the data in question in order to estimate the red noise and search for higher frequency periodic variations in the light curve. We generated a periodogram of the detrended data with and without the eclipse

**Table 2.** Qatar-1b parameters of the system from Covino et al. (2013) used in the analysis.

Parameter	Value
Planet-star radii ratio $R_p/R_*$	$0.1513 \pm 0.0008$
Transit epoch $T_0$ (days)	$2455518.41094 \pm 0.00016$
Transit duration $T_{1-4}$ (days)	$0.0678 \pm 0.0010$
Orbital period $P$ (days)	$1.42002504 \pm 0.00000071$
Orbital inclination $i$ (deg)	$83.82 \pm 0.25$
Semimajor axis $a$ (AU)	$0.02343 \pm 0.0012$
Stellar radius $R_*$ ( $R_\odot$ )	$0.80 \pm 0.05$
Planet radius $R_p$ ( $R_{\text{Jup}}$ )	$1.18 \pm 0.09$
Stellar $T_{\text{eff}}$ (K)	$4910 \pm 100$

(by removing the eclipse model obtained from the analysis presented in Sect. 3.2), and significant red noise was detected in timescales greater than  $\sim 6$  minutes for both cases. The average power at eclipse frequencies is  $\sim 9$  times the white noise.

### 3.2. A model for the secondary eclipse

We have performed a Markov chain Monte Carlo (MCMC) analysis in order to fit for Qatar-1b secondary eclipse, where we adopted the transit model from Mandel & Agol (2002), assuming no limb-darkening. Table 2 shows the orbital parameters used in the occultation model and in the analysis, published by Covino et al. (2013).

An initial modelling of the detrended unbinned light curve (with all 2850 individual measurements) was performed in order to define the initial conditions for the MCMC analysis, where we fit for three parameters: the eclipse depth ( $\Delta F$ ), a phase deviation ( $\Delta\phi$ ) of the eclipse in order to search for variations in time, what would imply a non-zero eccentricity, and the baseline level ( $F_{bl}$ ). This resulted in an eclipse depth,  $\Delta F$ , of 0.181%, a light curve baseline level,  $F_{bl}$ , at 1.0003, and a measured deviation in phase from mid-eclipse timing,  $\Delta\phi$ , of  $-0.0069$ .

We then perform the MCMC analysis of the uncorrected light curve, unifying the decorrelation function and the occultation model in a joint fit (hereafter joint-MCMC). This way, we were able to integrate the effect of the systematics into the uncertainty estimates, as in Cruz et al. (2015). We simultaneously fit for the secondary eclipse and the systematic effects, generating a model of the form

$$\text{model} = m_{\text{occ}} \times f_{\text{sys}}. \quad (4)$$

The occultation model is represented here by  $m_{\text{occ}}$ . The polynomial  $f_{\text{sys}}$  is given by Eq. 3, however it is calculated for the whole light curve, including the data during the eclipse. We considered the values defined previously for the eclipse model as initial conditions, except for the baseline level, which was kept fixed at  $F_{bl} = 1.0$ . The coefficients obtained by the linear regression (Sect. 3.1) were also used as initial conditions.

We ran four chains of  $1.1 \times 10^6$  simulations each. The first  $1 \times 10^5$  simulations from each chain were neglected, so that the analysis is not directly influenced by the initial conditions. In total, we have generated  $4 \times 10^6$  models, considering the simulations from all four chains. From this analysis, we obtained an eclipse depth of  $0.186\%^{+0.0006}_{-0.024\%}$  in flux, and a deviation in phase of  $-0.0071^{+0.0006}_{-0.0010}$ , given by median in the distributions from the joint-MCMC analysis. The uncertainties were determined by the 16-84% interval of the joint-MCMC parameter distribution. The convergence of the MCMC chains are at  $10^{-4}$  for the phase shift and at  $10^{-5}$  for the depth of the eclipse.

<sup>5</sup> Since we have used a fixed aperture (12.5 pixels) for the whole data set, a correction was estimated by defining a new radius around the target centered from a boundary of 4 sigma above the residual background, for each image individually. From this new radius, we have obtained the “defocused seeing” by multiplying it by the plate scale.

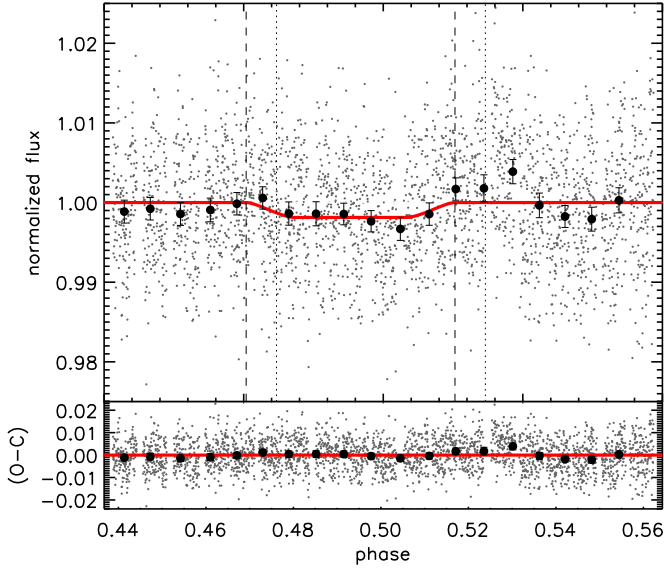


**Fig. 3.** Secondary eclipse of Qatar-1b in the Ks-band, showing the best fitting model with  $\Delta F = 0.186\%$ , and  $\Delta\phi = -0.0071$ . The detrended light curve is presented, where the small dots show the individual measurements. The solid line represents the best occultation model obtained from the joint-MCMC analysis, after removing the contribution of the systematics. The dotted vertical lines show the ingress and egress positions expected for circular orbit, and the dashed lines present ingress and egress found in the analysis. The filled circles show the light curve binned every 143 points ( $\sim 9.5$  minutes), for a better visualization.

Figure 3 presents the best occultation model from the joint-MCMC for the unbinned light curve, after removing the contribution of the systematics. The dotted vertical lines show the ingress and egress positions expected for the secondary eclipse considering a circular orbit, and the dashed lines present the deviation in phase found in the analysis.

Since the red noise present in the data is not negligible (see Sect. 3.1), we have used the “Prayer Bead” method (Moutou et al. 2004, Gillon et al. 2007) to assess the impact of red noise on the derived parameters. We have revised the uncertainties from the distribution of the values obtained from MCMC simulations with the “Prayer Bead” method (hereafter PB-MCMC). Here, we first shift sequentially the residuals of the joint-MCMC fit and then add the best fit occultation model. In this way, we have generated as many light curves as residual permutations that went through the same MCMC procedure.

From the distribution of values obtained from the PB-MCMC, we derived an eclipse depth of  $0.196\%^{+0.071\%}_{-0.051\%}$  and a phase shift of  $-0.0079^{+0.0162}_{-0.0043}$  ( $-16.15^{+33.12}_{-8.79}$  minutes). Again, the uncertainties were determined by the 16-84% interval of the PB-MCMC parameter distribution. We note that we have a limited sample of red noise, and its timescale is comparable with the eclipse duration, which could compromise the shape of the distributions obtained from the PB-MCMC analysis, and may yield an overestimation of the derived uncertainties.

## 4. Discussion

### 4.1. Derived orbital configuration

Based on the observation of a phase offset, it was possible to investigate possible intervals for the eccentricity,  $e$ , and the argument of periastron,  $\omega$ , by following the relationship (Wallenquist

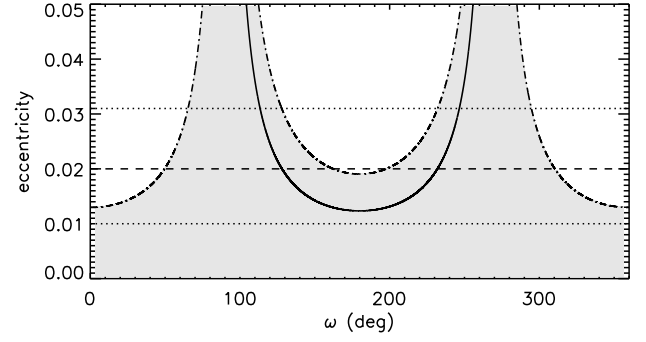


**Fig. 4.** Distinct orbital configurations for  $e \cos \omega = -0.0123^{+0.0252}_{-0.0067}$ , with the value  $e \cos \omega = -0.0123$  presented as a solid line. The lower and upper limits are shown as dash-dotted lines. The whole interval of  $-0.0190 \leq e \cos \omega \leq 0.0129$  is represented by the gray shaded area. The horizontal dotted lines show the eccentricity range found by Covino et al. (2013), with  $e = 0.02$  presented as a dashed horizontal line.

1950, López-Morales et al. 2010):

$$e \cos \omega = \pi \cdot \frac{\delta\phi - 0.5}{1 + \csc^2(i)}, \quad (5)$$

where  $\delta\phi = \phi_{ecl} - \phi_{tra}$ , and  $i$  is the orbital inclination of the system. The phase of the secondary eclipse is defined as  $\phi_{ecl} = 0.5 + \Delta\phi$ .

We have derived a phase offset for the Qatar-1b system of  $\Delta\phi = -0.0079^{+0.0162}_{-0.0043}$ , which combined with Qatar-1b’s orbital inclination (shown in Table 2) results in a value for  $e \cos \omega$  of  $-0.0123^{+0.0252}_{-0.0067}$ , from the equation above. This value of  $e \cos \omega$  can lead to several combinations of  $e$  and  $\omega$ , consistent with a near-to-circular orbit configuration.

Figure 4 presents possible  $e$  and  $\omega$  combinations suitable for the estimated  $e \cos \omega$ , where the value  $e = -0.0123$  is shown as a solid line, and the lower and upper limits are presented as dash-dotted lines. All possible combinations are represented by the gray shaded area. With high precision RV measurements, Covino et al. (2013) determined a small eccentricity of  $e = 0.020^{+0.011}_{-0.010}$ . Their result is shown as dashed and dotted horizontal lines in Fig. 4, as the range of possible eccentricities ( $0.010 \leq e \leq 0.031$ ). Based on our derived  $e \cos \omega$  and its uncertainties, it is not possible to constrain  $\omega$  for eccentricities lower than 0.02.

It is worth noting that the derived  $e \cos \omega$  in this work should be further investigated with additional data.

### 4.2. Thermal emission of Qatar-1b

From the secondary eclipse depth we can also derive the brightness temperature of Qatar-1b in the Ks-band,  $T_{Ks}$ . As presented in Sect. 3.2, we measured an eclipse depth (i.e., flux ratio at a given wavelength) of  $\Delta F = 0.196\%^{+0.071\%}_{-0.051\%}$ . Considering the parameters in Table 2 and assuming that Qatar-1b and its central star emit as black-bodies, we can estimate a Ks-band brightness temperature of  $T_{Ks} \approx 1885^{+212}_{-168}$  K.

Assuming an inefficient energy circulating atmosphere ( $f = 2/3$ ) and a zero Bond albedo ( $A_B = 0$ ), we would expect a maximum equilibrium temperature<sup>6</sup> for this exoplanet of  $T_{eq} \approx 1768$

<sup>6</sup>  $T_{eq} = T_s \cdot (R_s/a)^{1/2} \cdot [f \cdot (1 - A_B)]^{1/4}$ .  $T_s$  and  $R_s$  are the stellar effective temperature and radius,  $a$  is the orbital semimajor axis,  $f$  is the energy reradiation factor and  $A_B$  is the planet’s Bond albedo.

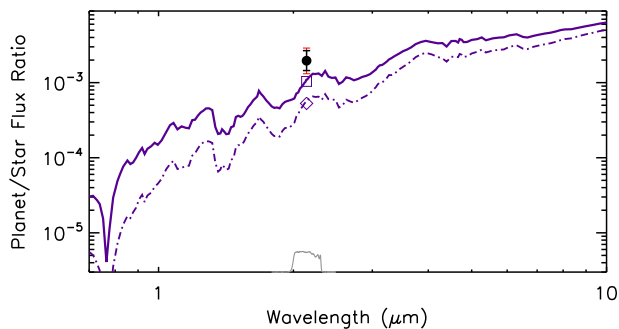


**Fig. 5.** Model spectrum of thermal emission of Qatar-1b with a reradiation factor of  $f = 2/3$ , without TiO/VO (solid line). The filled circle shows the measured planet-to-star flux ratio, in the Ks-band ( $\lambda_c = 2.14 \mu\text{m}$ ). The error bar shown in red represents the expected flux ratio for a temperature range of  $T_{\text{Ks}} \pm 200 \text{ K}$ . The dot-dash line illustrates a similar model, with  $f = 1/2$ . The Ks-band transmission curve (gray line) is shown at the bottom of the panel at arbitrary scale.

K. In this case, the derived Ks-band brightness temperature ( $T_{\text{Ks}}$ ) of Qatar-1b is in agreement with the maximum estimated  $T_{\text{eq}}$ , within the error estimates.

Some studies suggest that an opacity source, e.g., TiO and VO, in a high layer of a planet’s atmosphere can lead to a hot stratosphere and hence to a temperature inversion layer. According to Fortney et al. (2006), atmospheric models with a temperature inversion would show a weak emission in the near-infrared (JHK bands), and stronger emissions would be present in models without such inversion layer, at the same wavelength bands. The measured planet-to-star flux ratio, given by the eclipse depth, was then compared with several atmospheric spectral models by Fortney et al. (2006, 2008). These models were generated considering different reradiation factors ( $f$ ), and computed without TiO/VO, since such models tend to have higher K-band fluxes.

Figure 5 shows, as an example, the atmospheric spectral model that better represents the observed thermal emission of Qatar-1b. This model, shown as a solid line, was generated considering an instant reradiation over the dayside ( $f = 2/3$ ), and it was calculated without TiO/VO. Although, it can not reproduce the measured planet-to-star flux ratio (filled circle), the high observed  $T_{\text{Ks}}$  suggests an extremely inefficient redistribution onto the night side, or missing physics in the atmosphere model, since the planet is hotter than the hottest ( $f = 2/3$ ) model.

The observed emission may suggest that Qatar-1b does not have a temperature inversion, if we assume the absence of TiO and VO in its atmosphere. Nevertheless, more observations would be needed, at different wavelengths, to allow a complete understanding of this exoplanet’s atmosphere, and to confirm or exclude the absence of an inversion layer.

Stellar activity may also explain the high observed brightness temperature of Qatar-1b. Khodachenko et al. (2007) presented that coronal mass ejections can interact with upper planetary atmospheres and may affect their temperature structure. In addition, constant UV flares and X-ray radiations may heat the exoplanet’s atmosphere and enhance atmospheric escape (Khodachenko et al. 2007, Lammer et al. 2007). Considering the proximity of Qatar-1b to its host star (0.02343 AU), such interactions should not be neglected.

Mislis et al. (2015) searched for signs of activity in the available photometric database. Since starspots are common on K-dwarfs, and may be responsible for a brightness modulation at

the stellar rotational period, they analyzed the survey photometry in Qatar-1b discovery paper in order to look for signs of spot activity. Their results showed a sinusoidal variation in the light curve interpreted to be due to the presence of spots. However, there was no evidence of starspot via occultation during the observed transits.

Hence, further analysis on the stellar activity is needed. The effect of such activity should also be investigated in order to characterize Qatar-1b’s atmosphere.

## 5. Conclusions

We have observed the secondary eclipse of Qatar-1b in the Ks-band. The observations were made in staring mode at the 3.5 m telescope at Calar Alto (Spain), equipped with the OMEGA2000 instrument.

The obtained light curve was treated with the same procedure described in Cruz et al. (2015). We used Principal Component Analysis to identify correlated systematic trends in the data. The following step was to perform a Markov chain Monte Carlo analysis in order to model the correlated systematics and fit for Qatar-1b secondary eclipse using the Mandel & Agol (2002) transit model. From this analysis, we obtained an eclipse depth ( $\Delta F$ ) of  $0.186\%^{+0.022\%}_{-0.024\%}$  in flux, and a deviation in phase from mid-eclipse ( $\Delta\phi$ ) of  $-0.0071^{+0.0006}_{-0.0010}$ . We adopted the “Prayer Bead” method in order to assess the impact of red noise on the derived parameters, which resulted in an eclipse depth of  $0.196\%^{+0.071\%}_{-0.051\%}$ , and a deviation in phase of  $-0.0079^{+0.0162}_{-0.0043}$ .

The observed phase shift leads to a value for  $e \cos \omega$  of  $-0.0123^{+0.0252}_{-0.0067}$ , which should be confirmed with more data. The planet-to-star flux ratio observed resulted in a brightness temperature in the Ks-band of  $T_{\text{Ks}} \approx 1885^{+212}_{-168} \text{ K}$ , which is in agreement with the maximum equilibrium temperature of  $T_{\text{eq}} \approx 1768 \text{ K}$ , within the error estimates. Further analysis on the stellar activity and a study of the effect of such activity on Qatar-1b should be performed in order to characterize the atmosphere of this close orbiting exoplanet.

**Acknowledgements.** This research has been funded by Spanish grants AYA2012-38897-C02-01, and PRICIT-S2009/ESP-1496. PC, DB, and JB have received support from the RoPACS network during this research, a Marie Curie Initial Training Network funded by the European Commissions Seventh Framework Programme. J.L-B acknowledges financial support from the Marie Curie Actions of the European Commission (FP7-COFUND) and the Spanish grant AYA2012-38897-C02-01. This work was performed in part under contract with the California Institute of Technology (Caltech)/Jet Propulsion Laboratory (JPL) funded by NASA through the Sagan Fellowship Program executed by the NASA Exoplanet Science Institute. This article is based on data collected under Service Time program at the Calar Alto Observatory, the German-Spanish Astronomical Center, Calar Alto, jointly operated by the Max-Planck-Institut für Astronomie Heidelberg and the Instituto de Astrofísica de Andalucía (CSIC). We are very grateful to the CAHA staff for the super quality of the observations. This work has made use of the ALADIN interactive sky atlas and the SIMBAD database, operated at CDS, Strasbourg, France, and of NASA’s Astrophysics Data System Bibliographic Services.

## References

- Alsubai, K. A., Parley, N. R., Bramich, D. M., et al., 2011, MNRAS, 417, 709
- Carter, J. A., & Winn, J. N., 2009, ApJ, 704, 51
- Covino, E., Esposito, M., Barbieri, M., et al., 2013, A&A, 554, A28
- Croll, B., Albert, L., Lafreniere, D., et al., 2010a, ApJ, 717, 1084
- Croll, B., Jayawardhana, R., Fortney, J. J., et al., 2010b, ApJ, 718, 920
- Croll, B., Lafreniere, D., Albert, L., et al., 2011, AJ, 141, 30
- Cruz, P., Barrado, D., Lillo-Box, J., et al., 2015, A&A, 574, A103
- de Mooij, E. J. W., de Kok, R. J., Nefs, S. V., Snellen, I. A. G., 2011, A&A, 528, A49
- Fortney, J. J., Saumon, D., Marley, M. S., et al., 2006, ApJ, 642, 495

- Fortney, J. J., Lodders, K., Marley, M. S., et al., 2008, *ApJ*, 678, 1419  
 Gillon, M., Demory, B.-O., Barman, T., et al., 2007, *A&A*, 471, L51  
 Khodachenko, M. L., Ribas, I., Lammer, H., et al., 2007, *Astrobiology*, 7, 167  
 Lammer, H., Lichtenegger, H. I. M., Kulikov, Y. N., et al., 2007, *Astrobiology*, 7, 185  
 Liddle, A. R. 2007, *MNRAS*, 377, L74  
 López-Morales, M., & Seager, S., 2007, *ApJ*, 667, L191  
 López-Morales, M., Coughlin, J. L., Sing, D. K., et al., 2010, *ApJ*, 716, L36  
 Maciejewski, G., Fernández, M., Aceituno, F. J., et al., 2015, *arXiv:1503.07191v1*  
 Mandel, K., Agol, E., 2002, *ApJ*, 580, L171  
 Mislis, D., Mancini, L., Tregloan-Reed, J., et al., 2015, *MNRAS*, 448, 2617  
 Morrison, D. F., 1976, *Multivariate Statistical Methods*. McGraw-Hill Book Co., Singapore  
 Moutou, C., Pont, F., Bouchy, F., Mayor, M., 2004, *A&A*, 424, L31  
 Schwarz G., 1978, *Ann. Statist.*, 6, 461  
 von Essen, C., Schröter, S., Agol, E., Schmitt, J. H. M. M., 2013, *A&A*, 555, A92  
 Wallenquist, Å., 1950, *Ark. Astron.*, 1, 59

## Appendix A: Behavior of selected baseline parameters

Figure A.1 shows the xy-position of the centroid at the detector, the “defocused seeing” (defined previously in Sect. 3.1), and the airmass as function of phase, in order to illustrate the behavior of the baseline selected parameters over time. Here, the first two plots show the variation of the position of the star, which is in fact the centroid’s position minus the median of the position of the star overnight, in pixels. The “seeing” is presented in arcsec.

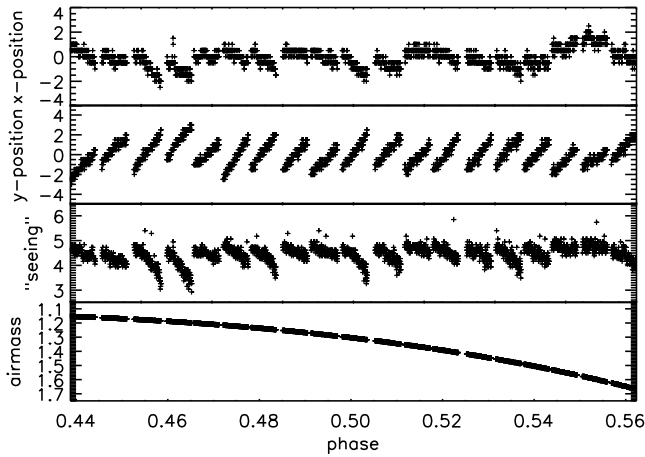


**Fig. A.1.** Behavior of the xy-position of the centroid at the detector (in pixels), the “defocused seeing” (in arcsec), and the airmass as function of phase.